

## MATERIALS SCIENCE

# Controlling magnetoresistance by tuning semimetallicity through dimensional confinement and heteroepitaxy

Shouvik Chatterjee<sup>1,2\*</sup>, Shoaib Khalid<sup>3,4</sup>, Hadass S. Inbar<sup>5</sup>, Aranya Goswami<sup>1</sup>, Taozhi Guo<sup>6</sup>, Yu-Hao Chang<sup>5</sup>, Elliot Young<sup>5</sup>, Alexei V. Fedorov<sup>7</sup>, Dan Read<sup>1,8</sup>, Anderson Janotti<sup>3\*</sup>, Chris J. Palmstrøm<sup>1,5,9\*</sup>

Copyright © 2021  
The Authors, some  
rights reserved;  
exclusive licensee  
American Association  
for the Advancement  
of Science. No claim to  
original U.S. Government  
Works. Distributed  
under a Creative  
Commons Attribution  
NonCommercial  
License 4.0 (CC BY-NC).

Controlling electronic properties via band structure engineering is at the heart of modern semiconductor devices. Here, we extend this concept to semimetals where, using LuSb as a model system, we show that quantum confinement lifts carrier compensation and differentially affects the mobility of the electron and hole-like carriers resulting in a strong modification in its large, nonsaturating magnetoresistance behavior. Bonding mismatch at the heteroepitaxial interface of a semimetal (LuSb) and a semiconductor (GaSb) leads to the emergence of a two-dimensional, interfacial hole gas. This is accompanied by a charge transfer across the interface that provides another avenue to modify the electronic structure and magnetotransport properties in the ultrathin limit. Our work lays out a general strategy of using confined thin-film geometries and heteroepitaxial interfaces to engineer electronic structure in semimetallic systems, which allows control over their magnetoresistance behavior and simultaneously provides insights into its origin.

## INTRODUCTION

Semimetallic compounds offer an exciting platform to realize exotic quantum states of matter and novel material properties (1–4). Large, nonsaturating magnetoresistance is one such example (5–11), where spin-orbit coupling (5, 6), linearly dispersive states (8), charge compensation (9, 10), and disorder effects (11) have been proposed as possible mechanisms for its origin. Although electronic structure is expected to play a key role, demonstration of controlling the magnetoresistance via electronic structure modification remains elusive, which might allow us to distinguish between the different proposed scenarios. To address this outstanding issue, we fabricated epitaxial thin films of a semimetallic compound LuSb on GaSb substrates with different film thicknesses. Although LuSb is found to be a compensated semimetal in the bulk (12, 13), we establish that dimensional confinement differentially alters the occupation of electron and hole-like bands lifting carrier compensation. Loss of carrier compensation along with an overall reduction in carrier mobility in thinner films markedly modifies their magnetoresistance behavior establishing the importance of carrier compensation. However, no evidence is found for the predicted semimetallic to semiconducting phase transition (14) in dimensionally confined thin films of LuSb, which remain semimetallic in the ultrathin limit.

Heteroepitaxial interfaces offer another potential avenue to control electronic properties in few atomic layer geometries and can lead to emergent ground states not realizable in the bulk (15–17). We show that the nature of the local coordination and chemical bonding at a heterointerface provides a novel route to realize a two-dimensional (2D) electron/hole gas. In particular, the heterointerface between a rock-salt (LuSb) and zinc-blende (GaSb) crystal structures results in the emergence of a 2D hole gas that remains tightly bound to the interface and is accompanied by a charge transfer across it, substantially affecting the electronic structure and transport properties in LuSb in the ultrathin limit.

## RESULTS AND DISCUSSION

### Growth and transport

Epitaxial thin films of rock-salt LuSb (6.055 Å) (18) were synthesized on a nearly lattice-matched GaSb substrates (6.096 Å) with a thin GaSb epitaxial buffer layer using molecular-beam epitaxy (MBE). The  $c(2 \times 6)$  reconstruction of the Sb-rich GaSb(001) surface immediately changes to a  $(1 \times 1)$  reconstruction at the beginning of the deposition of LuSb atomic layers, shown in Fig. 1B. The LuSb atomic layers remain epitaxial and single phase with [001] out-of-plane orientation even in the ultrathin limit, as revealed by the  $\theta$  to  $2\theta$  x-ray diffraction scans shown in Fig. 1C. Details about further structural characterization of these films can be found in (19) (section S1 and fig. S1).

Dimensional confinement is found to significantly modify electrical properties of LuSb, which is a semimetal in the bulk with hole pockets ( $\beta$  and  $\delta$ ) at the zone center and an elliptical electron pocket at the zone edge ( $\alpha$ ), as shown in Fig. 1A. While the 40-, 32-, and 20-monolayer (ML)-thick films exhibit metallic behavior, a low temperature resistivity upturn can be seen in the 12-, 8-, and 6-ML-thick films (Fig. 1D). At high temperatures, parallel conduction from the underlying GaSb buffer layers and GaSb substrate strongly influences temperature dependence of film resistance in the LuSb/GaSb

<sup>1</sup>Department of Electrical and Computer Engineering, University of California, Santa Barbara, CA 93106, USA. <sup>2</sup>Department of Condensed Matter Physics and Materials Science, Tata Institute of Fundamental Research, Homi Bhabha Road, Mumbai 400005, India. <sup>3</sup>Department of Materials Science and Engineering, University of Delaware, Newark, DE 19716, USA. <sup>4</sup>Department of Physics and Astronomy, University of Delaware, Newark, DE 19716, USA. <sup>5</sup>Materials Department, University of California, Santa Barbara, CA 93106, USA. <sup>6</sup>Department of Physics, University of California, Santa Barbara, CA 93106, USA. <sup>7</sup>Advanced Light Source, Lawrence Berkeley National Laboratory, Berkeley, CA 94720, USA. <sup>8</sup>School of Physics and Astronomy, Cardiff University, Cardiff CF24 3AA, UK. <sup>9</sup>California NanoSystems Institute, University of California, Santa Barbara, CA 93106, USA.

\*Corresponding author. Email: shouvik.chatterjee@tifr.res.in (S.C.); janotti@udel.edu (A.J.); cjpalm@ucsb.edu (C.J.P.)

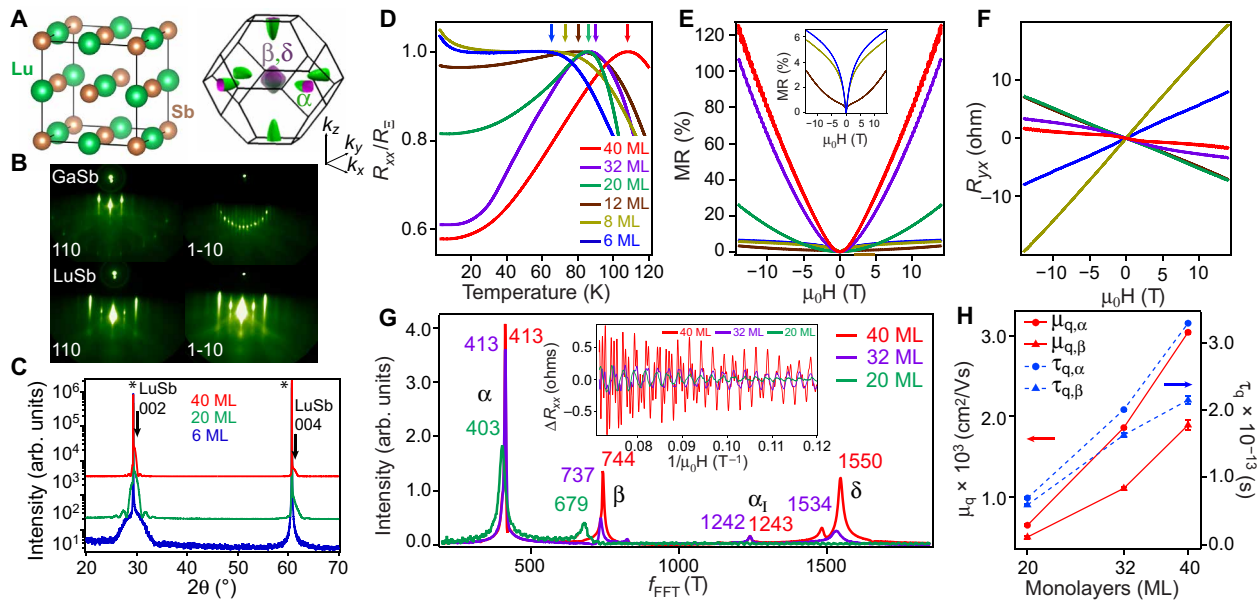


**Fig. 1. Synthesis and transport properties of LuSb/GaSb (001) thin films.** (A) Crystal structure of LuSb and its Fermi surface, calculated using hybrid DFT. (B) Reflection high-energy electron diffraction (RHEED) images along the [110] and [1-10] azimuths. (C) Out-of-plane  $\theta$ -2 $\theta$  x-ray diffraction (XRD) scans for epitaxial films of different thicknesses studied in this work. Substrate peaks are marked by asterisks. XRD scans are offset in intensity (along the y axis) for clarity. (D) Temperature dependence of resistance in thin films of various thicknesses.  $R_{\Sigma}$  is the resistance at the sample temperature below which film resistance is dominated by LuSb layer. Temperatures corresponding to  $R_{\Sigma}$  are indicated for all film thicknesses. (E) Evolution of magnetoresistance with film thickness. Inset highlights saturating magnetoresistance behavior at high fields for 8- and 6-ML-thick samples. All data taken at 2 K. (F) Hall resistance measured at 2 K as a function of film thickness. (G) Fast Fourier transform of the quantum oscillations for the 40-, 32-, and 20-ML-thick films. Corresponding resistance oscillations are shown in the inset.  $\beta$  and  $\delta$  are the hole pockets at the zone center.  $\alpha$  and  $\alpha_1$  are the frequencies corresponding to the projection of the elliptical electron pockets along the magnetic field direction ( $k_z$ ) and those lying in the plane perpendicular to it ( $k_x$  and  $k_y$ ), respectively, as shown in (A). (H) Extracted quantum mobility and carrier lifetime for the  $\alpha$  and  $\beta$  pockets for the 40-, 32-, and 20-ML-thick films.

thin films. Charge carriers in GaSb freeze out at low temperatures resulting in the film resistance being dominated by the LuSb atomic layers, which is the region of interest in this study [see fig. S2 (19)]. The temperature at which resistance of LuSb atomic layer starts to dominate depends on the relative resistance of the LuSb atomic layer in comparison to that of GaSb, which depends on the LuSb film thickness. To compare temperature dependence of the longitudinal resistance in thin films with different LuSb layer thicknesses, we show normalized resistance  $R_{xx}/R_{\Sigma}$  in Fig. 1D, where  $R_{\Sigma}$  is the resistance below which the film resistance is dominated by the LuSb atomic layer as is evident from a marked change in slope as a function of temperature.  $R_{\Sigma}$  for different film thicknesses are shown by corresponding arrows in Fig. 1D. Magnetoresistance in these films also undergo marked changes both in magnitude and shape with film thickness (Fig. 1E). While the 40-ML-thick film exhibits a MR of 120% at 14 T, it drops down to less than 10% in the thinner films. Furthermore, the 8- and 6-ML-thick films show a saturating behavior at high field values unlike the thicker films due to strong electron-electron interaction (EEI) effects [fig. S2 (19)]. Shubnikov de Haas (SdH) oscillations were observed in the magnetoresistance data, shown in Fig. 1E, for all the electronic bands ( $\alpha$ ,  $\beta$ , and  $\delta$ ) for the 40- and 32-ML-thick films, but only for the  $\alpha$  and  $\beta$  bands for the 20-ML-thick film, and were absent in the thinner films, indicating an overall reduction in mobility with decreasing film thickness (Fig. 1, E and G). A smooth fifth-order polynomial background was used to extract SdH oscillations from the magnetoresistance data, shown in Fig. 1G. Further details of the extraction procedure can be found in (19) (section S3 and fig. S3). Quantum mobilities for the  $\alpha$  and  $\beta$  bands

were found to decrease by 84 and 77%, respectively, with the decrease in film thickness from 40 to 20 ML, shown in Fig. 1H. Details of the estimation of quantum mobilities are provided in (19) (section S3 and fig. S4). The quantum oscillation measurements further indicate that dimensional confinement induces a change in the electronic structure of LuSb, differentially affecting the electron and hole-like bands. The Fermi wave vector ( $k_F$ ) for the hole-like  $\beta$  pocket was found to have reduced from 0.1504 to 0.1436  $\text{\AA}^{-1}$ , a change of  $\approx 0.007 \text{ \AA}^{-1}$ , on reduction of the layer thickness from 40 to 20 ML. However, for the electron-like  $\alpha$  pocket, the change in the Fermi wave vector along the semimajor axis was only from 0.112 to 0.1107  $\text{\AA}^{-1}$ , an insignificant change of  $\approx 0.001 \text{ \AA}^{-1}$ . This is also manifested in the Hall measurements where a multi-carrier Hall behavior in the 40- and 32-ML-thick films changes to a single carrier electron-like behavior in the thinner films of 20 and 12 ML (Fig. 1F; also see fig. S3), as evidenced from the linear Hall data for these films, up to a magnetic field of 14 T. This can be understood as the predominance of electron-like carriers over hole-like carriers in thinner films, consistent with the results from SdH oscillation analysis, indicating that, in thinner films, electron-hole compensation is lifted with a much larger concentration of electron-like carriers. However, unexpectedly in contrast to the thicker films, p-type Hall conductivity (positive slope of the Hall coefficient) is observed in the 8- and 6-ML-thick films, which is discussed later.

### Angle-resolved photoemission spectroscopy

To gain insights into our transport results, we directly map out the evolution of the electronic structure of LuSb with decreasing film

thickness by angle-resolved photoemission spectroscopy (ARPES). The measurements were taken at a photon energy of 60 eV, which samples a 2D momentum region ( $k_x, k_y$ ) of the 3D Brillouin zone with  $k_z$  close to the bulk  $\Gamma$  point (see Fig. 2A). The Fermi surface of LuSb showing both the hole pockets ( $\beta$  and  $\delta$ ) at the zone centre ( $\Gamma$ ) and the elliptical electron pocket ( $\alpha$ ) at the zone edge ( $X$ ) is shown in Fig. 2B. In Fig. 2 (C to J), we show the hole and the electron pockets at the  $\Gamma$  and the bulk  $X$  points ( $\bar{M}$  at the surface Brillouin zone), respectively, for different film thicknesses. The occupation of the hole pockets decreases markedly as the film thickness is reduced, whereas no apparent change in occupation of the electron pocket is observed for all but 6-ML-thick film. For the 6-ML-thick film, we observe a slight reduction in ellipticity ( $e = \frac{k_{F, \text{semimajor}}}{k_{F, \text{semiminor}}}$ ) of the electron pocket

with  $k_{F, \text{semiminor}}$  remaining unchanged from the bulk limit. Finite thickness of our films results in the formation of quantum well states observed for the hole-like carriers in the 20-, 12-, and 6-ML-thick samples (Fig. 2, C to F). We, however, do not observe the corresponding quantum well states for the electron pocket (Fig. 2, G to J). This is most likely due to finite lateral coherence length in our thin films coupled with the fact that an off-normal geometry with a high polar angle had to be used in the ARPES measurements of the electron pocket due to their location at the zone edge (see Fig. 1A) (20).

We estimated Fermi wave vectors ( $k_F$ ) of all the Fermi surface sheets ( $\alpha$ ,  $\beta$ , and  $\delta$ ) from the ARPES data, shown in Fig. 2 (C to J), from where corresponding carrier concentration was estimated noting that the  $\beta$  and  $\delta$  bands are quasi-spherical ( $n_{3D} = \frac{k_F^3}{3\pi^2}$ ), while the  $\alpha$  band is elliptical ( $n_{3D} = \frac{k_{F, \text{semiminor}}^2 k_{F, \text{semimajor}}}{3\pi^2}$ ) (see Figs. 1A and 2B). Extracted  $k_F$ s for different film thicknesses are shown in Fig. 3B (also see fig.

S5). While the 40-ML-thick film, which is in the bulk limit, is a compensated semimetal with near-equal concentration of electron ( $n = 3.22 \times 10^{20} \text{ cm}^{-3}$ ) and hole-like carriers ( $p = 3.18 \times 10^{20} \text{ cm}^{-3}$ ) with a ratio  $\frac{n}{p} \approx 1.01$ , thinner films are not carrier compensated with the effect being exacerbated as the film thickness is reduced. For the 6-ML-thick film, we observe two occupied subbands for the  $\delta$  pocket and a single subband for the  $\beta$  pocket with an effective hole-like sheet carrier concentration of  $5.97 \times 10^{13} \text{ cm}^{-2}$ . Even considering finite occupation for only the lowest subband of just the in-plane electron pockets (i.e., those along  $k_x$  and  $k_y$ , with confinement along  $k_z$ ; see Fig. 1A), we obtain electron-like sheet carrier concentration of  $9.58 \times 10^{13} \text{ cm}^{-2}$  with the ratio  $\frac{n}{p} \approx 1.6$ , which is a conservative lower bound but is still far away from electron-hole compensation. Hence, the modification in the magnetoresistance behavior in LuSb thin films can be directly ascribed to the loss of electron-hole compensation in thinner atomic layers. Furthermore, no band inversion is observed in our measurements showing that topological aspects of the band structure are not important for the magnetoresistance in LuSb.

To understand the origins of the thickness-dependent changes of the electronic structure observed in our thin films, we performed slab calculations of LuSb using density functional theory (DFT). Details of the calculations can be found in Materials and Methods and in (19) (section S4 and figs. S7 to S9). Our calculations predict lifting of the electron-hole compensation in thinner films due to a differential reduction in the occupation of the electron and hole-like carriers with film thickness, in accordance with our experimental observation. However, the electron pocket ( $\alpha$ ), at  $\bar{M}$ , is also strongly affected by quantum confinement in our calculations (Fig. 3A), contrary to the experimental data shown in Fig. 3B. This apparent discrepancy stems from the additional interfacial effects and the resulting charge transfer into the LuSb atomic layers across the LuSb/GaSb interface (see Fig. 3C), the presence of which is revealed in our

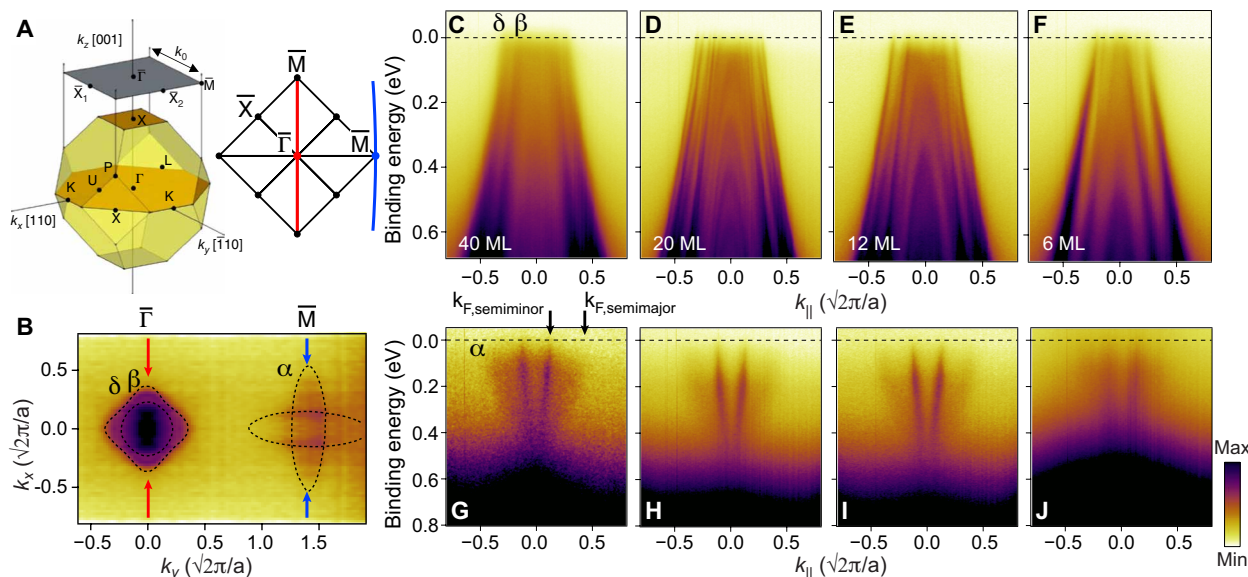


**Fig. 2. Photoemission spectroscopy of LuSb/GaSb (001) thin films.** (A) 3D and surface Brillouin zone of LuSb showing the high-symmetry points. Red and blue lines show the cut directions along which ARPES measurements are taken for (C) to (F) and (G) to (J), respectively. (B) Fermi surface map of bulk LuSb (12 ML) showing both the electron and the hole pockets and the ARPES cut directions. Calculated Fermi surface obtained from DFT using screened hybrid functional (HSE06) is shown by black dotted lines.  $E$ - $k$  spectral map at the bulk  $\Gamma$  point (top) along  $\bar{M} - \bar{\Gamma} - \bar{M}$  [red line in (A)] of the surface Brillouin zone for thin films of thickness (C) 40 ML, (D) 20 ML, (E) 12 ML, and (F) 6 ML and at the bulk  $X$  point (bottom) along  $\bar{\Gamma} - \bar{M} - \bar{\Gamma}$  [blue line in (A)] of the surface Brillouin zone for (G) 40-ML-, (H) 20-ML-, (I) 12-ML-, and (J) 6-ML-thick films. All data taken at 70 K and a photon energy of 60 eV.



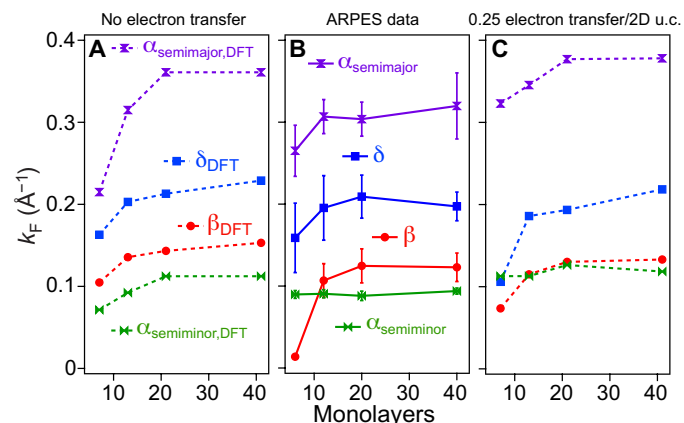


**Fig. 3. Evolution of Fermi wave vectors ( $k_F$ ) with film thickness.** Fermi wave vectors for both the elliptical electron-like pocket ( $\alpha$ ) and quasi-spherical hole-like pockets ( $\beta$  and  $\delta$ ) as a function of film thickness obtained from (A) LuSb slab calculation without considering charge transfer across the LuSb/GaSb interface, (B) ARPES measurements, and (C) LuSb slab calculations after adding a charge transfer of 0.25 electrons per 2D surface unit cell (u.c.) into the LuSb atomic layers (see text).

slab calculations when the substrate, GaSb, is also included, as discussed in the next section.

### Role of the interface

While the ARPES and quantum oscillation measurements along with the LuSb slab calculations establish the loss of electron-hole compensation in thinner films, dimensional confinement alone is not sufficient to explain all aspects of our experimental data. First, our observation of a positive Hall coefficient in the thinner films of 8 and 6 ML is in apparent contradiction to the ARPES and quantum oscillation measurements that show a larger carrier concentration of the electron-like carriers compared to hole-like carriers in these films. Second, evolution of the electron-like  $\alpha$  pocket with film thickness could not be reproduced by slab calculations when only LuSb atomic layers were considered, as noted earlier.

To understand the origins of these seemingly contradictory behaviors, we evaluate the nature of the interface in our thin-film heterostructure. A change in sign of the Hall coefficient from negative to positive values in thinner films could arise if the interface between LuSb and GaSb hosts a 2D hole gas, which will become increasingly important, and manifest in transport measurements in the ultrathin limit having a contribution comparable to that of the bulk film. To explore this scenario, we have fitted the transport data with a three-component Drude conductivity model

$$G_{xx} = \frac{R_{xx}}{R_{xx} + R_{xy}} = \frac{en_e\mu_e t + en_h\mu_h t + en_{2D}\mu_{2D}}{R_{xx} + R_{xy}} \quad (1)$$

$$G_{xy} = \frac{R_{xy}}{R_{xx} + R_{xy}} = B \times [-en_e\mu_e^2 t + en_h\mu_h^2 t + en_{2D}\mu_{2D}^2]$$

where the first and the second terms on the right-hand side represent contributions from the bulk of the film for the electron and hole-like carriers, respectively. The third term represents contribution from the interfacial state.  $n$ ,  $\mu$ , and  $t$  represent carrier concentration, mobility, and film thickness, respectively.  $G_{xx}$  and  $G_{xy}/B$  follow approximately  $t^2$  and  $t^3$  behaviors, respectively, between 12 and 32 ML and saturate for film thicknesses less than 12 ML, as

shown in Fig. 4 (B and C). The value to which the conductivity value saturates represents the contribution of the interfacial charge carriers from which we obtain an interfacial carrier concentration of  $n_{2D} = 4.38 \times 10^{14} \text{ cm}^{-2}$  ( $\approx 0.8$  holes per 2D unit cell) and a mobility of  $\mu_{2D} = 1.05 \text{ cm}^2/\text{Vs}$ . Furthermore, our analysis indicates that the mean free path and, hence, the mobility of the charge carriers in the bulk of the film for film thicknesses between 12 and 32 ML are primarily dominated by interfacial scattering and are thus proportional to the film thickness  $t$ . The 40-ML-thick film deviates from this trend, suggesting that at this thickness, the film is in the bulk 3D limit, which is in accordance with the absence of quantum well states in the ARPES measurements.

The existence of a 2D hole gas at the LuSb/GaSb (001) interface is revealed in our DFT slab calculations when the substrate GaSb is included. In Fig. 5A, we show the electronic band structure of the LuSb/GaSb/LuSb (001) slab. We find two interfacial bands crossing the Fermi level, mostly composed of  $s$  orbital of the Ga atoms at the interface, corresponding to one band with Ga- $s$  character per interface. These two bands show different dispersions along  $\Gamma - \bar{X}_1 - \bar{M}$  and  $\Gamma - \bar{X}_2 - \bar{M}$  because the corresponding Ga-Sb bonds at the two equivalent interfaces are rotated with respect to each other by  $90^\circ$  due to the symmetry of the zinc blende structure of GaSb. The Fermi-level crossings of these two bands and the resulting Fermi surface are shown in Fig. 5 (A and D), respectively, indicating a hole-like behavior, which explains experimental observation. The estimated carrier concentration, based on the Luttinger volume, is 0.7 hole per 2D unit cell area per interface. We note that the estimated Luttinger volume depends marginally on the functional used in the calculation and should be considered as a lower bound due to the use of generalized gradient approximation (GGA) in the slab calculations (see Materials and Methods). The calculated projected density of states, shown in (19) (fig. S9), also indicates that these interface bands are associated with the Ga atoms at the interface. The charge density distribution (Fig. 5B), corresponding to the square of the single-particle states at the maximum of the hole band along  $\bar{X}_2 - \bar{M}$  (highlighted by blue circles in Fig. 5A), reveals the 2D character of these two bands, which are highly localized out of plane yet uniformly distributed in the plane of the interface. Our calculations also predict distortion of the Lu atoms at the interface due to bonding mismatch, shown in Fig. 5E. This is directly observed in the high-angle annular

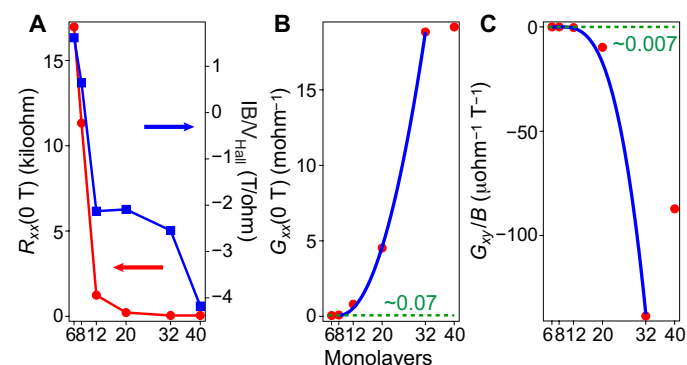


**Fig. 4. 2D hole gas at the LuSb/GaSb interface.** (A) Longitudinal resistance ( $R_{xx}$ ) at zero magnetic field and inverse of the slope in the Hall data, shown in Fig. 1F, as a function of film thickness. (B) Longitudinal conductance ( $G_{xx}$ ) and (C) transverse conductance coefficient ( $G_{xy}/B$ ), as defined in the text, as a function of film thickness. Saturation values of  $G_{xx}$  and  $G_{xy}/B$  are shown by green dotted lines.

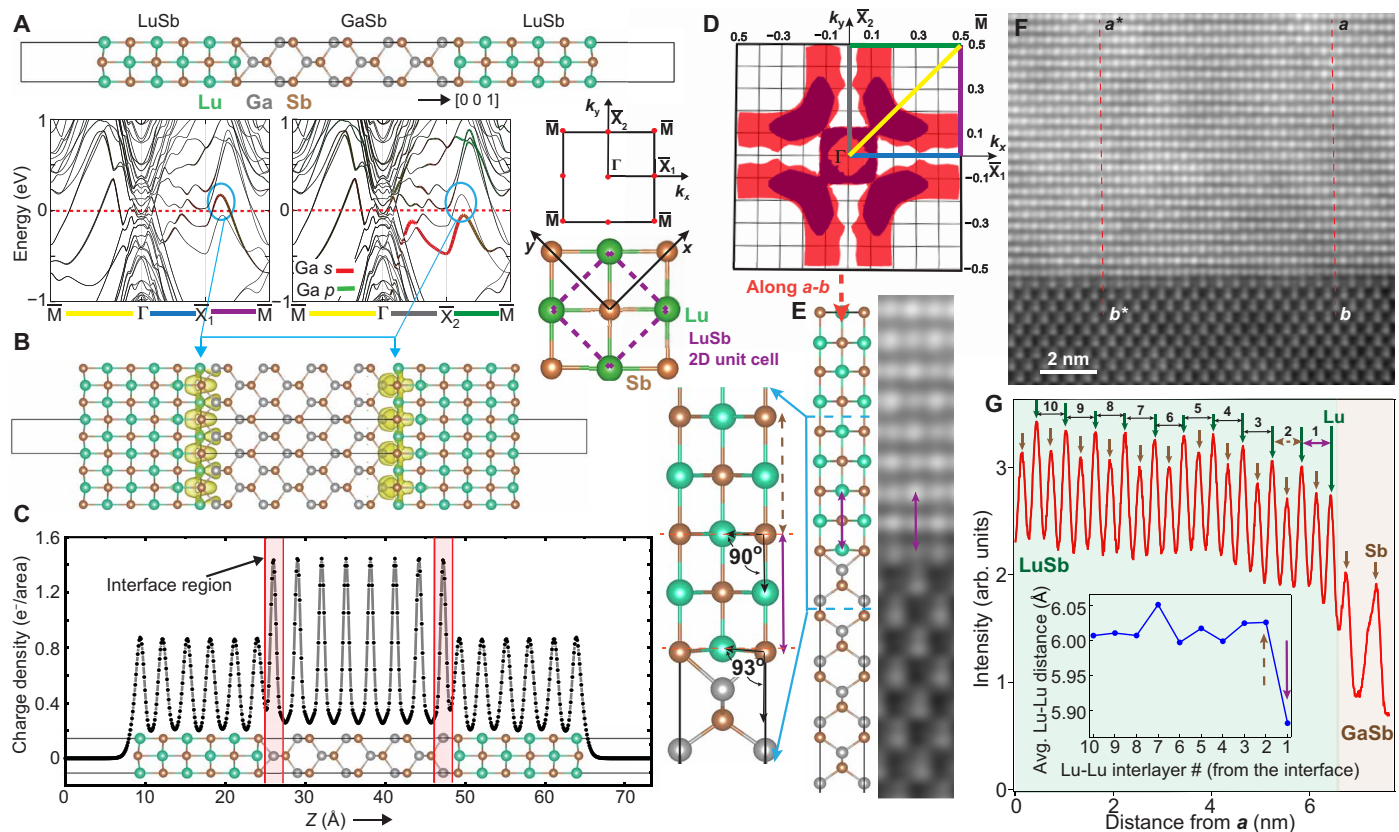


**Fig. 5. Origin of the 2D hole gas at a rock salt/zinc blende interface.** Electronic structure of a LuSb/GaSb/LuSb(001) slab showing (A) interface bands that originate from Ga s-orbitals at the interface. The 2D unit cell and the surface Brillouin zone are also shown. (B) Charge density distribution of the single-particle state at the maximum of the hole bands crossing the Fermi level along the  $\bar{X}_1 - \bar{M}$  and  $\bar{X}_2 - \bar{M}$  directions. (C) Valence charge density distribution of the LuSb/GaSb/LuSb (001) slab along the direction perpendicular to the interface. (D) Fermi surfaces of the two interface bands associated with the two equivalent interfaces, yet rotated, corresponding to the structure used in the simulation, shown in (A). (E) A close-up of the HAADF-STEM image in (F) and a ball-and-stick model of the proposed interface showing the atomic arrangement at the interface. (F) HAADF-STEM image along [110] zone axis. (G) Average atomic positions along  $a$ - $b$ , shown in (F), plotted as a function of the distance from  $a$ , calculated by averaging those atomic columns that terminate with a Lu atom at the interface between  $a$ - $b$  and  $a^*$ - $b^*$ . Inset shows the evolution of the Lu-Lu interatomic distance as a function of the distance from the interface. Lu-Lu interatomic pairs are numbered away from the interface, as shown. Distortion of the Lu atoms at the interface is evident from the change in bond angle in the calculations, shown in (E), which results in a reduced Lu-Lu interatomic distance between the first and the third LuSb monolayers (violet arrow) compared to the third and the fifth monolayers (brown dashed arrow).

dark-field scanning transmission electron microscopy (HAADF-STEM) data [see Fig. 5, E to G, and fig. S10 (19)], showing that the Lu-Lu interatomic distance in the out-of-plane direction is smaller at the interface, consistent with the predicted atomic layer buckling. This provides further evidence for the validity of our slab calculations in understanding the experimental results.

The charge density of this 2D hole gas and associated charge transfer to the LuSb atomic layers can also be estimated on the basis of a simple electron counting argument. In Fig. 5C, we show the valence charge density profile of the LuSb/GaSb/LuSb (001) slab system. The excess charge on the LuSb layer on the top or at the bottom of the GaSb layer is defined as the macroscopically averaged charge density along the heterostructure direction in the LuSb region (indicated in Fig. 5C) and the corresponding charge density of charge neutral LuSb bulk. The calculated excess charge density on the LuSb film amounts to 0.45 electrons per 2D interface unit cell area. Assuming that an excess charge of 1.5 electrons is expected at the interface due to the valence mismatch, i.e., in an ionic picture of GaSb, each Ga layer transfers 3/2 electrons to each of the neighboring

Sb layers, we obtain that  $1.5 - 0.45 = 1.05$  electrons per 2D unit cell area would remain at the interface. Discounting the electrons that are transferred to the bulk of GaSb, which is only 0.045 electrons per 2D unit cell area per interface according to the results shown in Fig. 5C, this will amount to  $\sim 1$  excess electron per 2D unit cell area per interface. Assuming that this electron partially occupies an interface band, we have about 1 hole per unit cell area in the interface band. This estimation of 1 hole per 2D unit cell can be considered as an upper bound value as GaSb bonds have strong covalent character.

The estimated range of 0.7 to 1 hole per 2D unit cell, based on the DFT calculations, corroborates the experimental value of 0.8 hole per 2D unit cell for the interface conducting channel obtained from the analysis of the Hall conductivity above. Furthermore, following our theoretical understanding, observation of 0.8 hole per 2D unit cell at the interface implies 0.25 excess electrons transferred to the LuSb atomic layers. Calculated  $k_F$  values for the LuSb slabs after inclusion of the charge transfer across the interface were found to be in close agreement with those extracted from ARPES, shown in Fig. 3C. This underscores the importance of the interfacial effects,

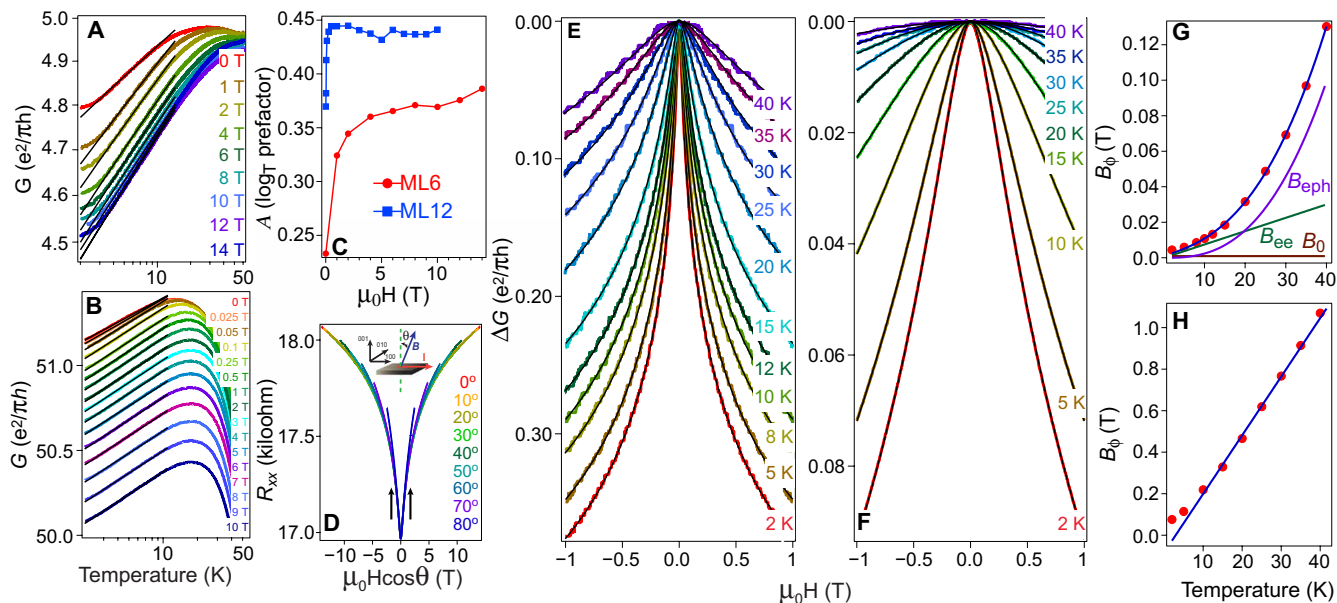


**Fig. 6. QI and EEI effects in ultrathin LuSb/GaSb (001) thin films.** Temperature dependence of conductance in (A) 6- and (B) 12-ML-thick films. Logarithmic fits to the conductance are shown in black. (C) Variation of the prefactor  $A$  (see Eq. 2), extracted from the fits in (A) and (B), as a function of applied magnetic field. (D) Resistance of a 6-nm-thick film plotted against the perpendicular component of the magnetic field vector for different angle values. The angle is defined in the inset. Arrows indicate that between  $\mu_0 H = \pm 1$  T, magnetoresistance curves obtained at different angular configurations fall on one another establishing the 2D nature of the QI effect. Differential conductance  $\Delta G(B = \mu_0 H) = G(B) - G(0)$  as a function of magnetic field and the corresponding HLN fits for (E) 12- and (F) 6-ML-thick films. Temperature dependence of the extracted dephasing field as a function of temperature for (G) 12- and (H) 6-ML-thick films. In (G), contributions of  $B_{ee}$ ,  $B_{eph}$ , and  $B_0$  to  $B_\phi$  are shown in green, violet, and brown, respectively.

in addition to the quantum confinement effects, in understanding the evolution of the electronic structure with film thickness in heteroepitaxial semimetallic thin films.

We note that an alternate explanation for the 2D hole gas at the LuSb/GaSb (001) interface could be due to band bending and surface accumulation in the GaSb interfacial layer resulting from the Fermi level at the GaSb surface being pinned in the valence band. We rule this out for the following reasons. First, the surface Fermi level pinning position of uncovered GaSb surfaces is known to lie 0.2 eV above the valence band (21). Second, both the photoemission results from metal/GaSb heterostructures and electrical measurements of metal/GaSb Schottky barriers indicate a surface Fermi level position within the GaSb bandgap (22–26). Last, the density of such electrostatically induced 2D hole gases is typically  $\leq 5 \times 10^{12}$  holes/cm<sup>2</sup> (27, 28), which is two orders of magnitude lower than the hole density observed in our experiments. Therefore, the 2D hole gas observed in our experiments is of novel origin arising due to bonding mismatch at the interface, which should be a generic feature of such heterointerfaces.

### Semimetal to semiconductor transition

The ARPES measurements shown in Fig. 2 clearly reveal that a finite occupation is maintained for both the electron and hole like bands, thereby preserving the semimetallic character of LuSb even at the ultrathin limit of 6 ML. This is at odds with the resistivity upturn at low temperatures observed in the transport measurements of the thinner films (Fig. 1D). In Fig. 6 (A and B), we show that the conductance drops logarithmically with temperature for the 6- and 12-ML-thick films, respectively

$$\Delta G(T) = \frac{e^2}{\pi h} A \ln\left(\frac{T}{T_0}\right) \quad (2)$$

where  $T_0$  is the reference temperature. This can arise from quantum interference (QI) effects such as weak localization and EEI in the 2D limit (29, 30). To distinguish between the two cases, we examine the change in slope in the temperature dependence of conductance as a function of applied magnetic field. QI effects can be readily suppressed on application of magnetic field, while EEI effects are more robust due to larger characteristic fields (29, 31). Therefore, the prefactor  $A$  in Eq. 2 obtained at high field values  $A_{\text{high}}$  is solely due to EEI effects  $A_{\text{high}} = A_{ee}$ , whereas the one at zero field is a combination of both QI ( $A_{\text{QI}}$ ) and EEI effects ( $A_{ee}$ ),  $A_{\text{low}} = A_{ee} + A_{\text{QI}}$ . We estimate  $A_{\text{QI}}$  to be  $-0.07$  and  $-0.15$  and  $A_{ee}$  equal to  $0.44$  and  $0.39$  for the 12- and 6-ML-thick films, respectively. We obtain a negative value for  $A_{\text{QI}}$  for both the 12- and 6-ML-thick films, consistent with the observation of weak antilocalization (WAL) behavior in magnetoresistance, shown in Fig. 6 (D to F). Angular dependence of magnetoresistance confirms the 2D character of WAL, while further distinguishing it from the effects of Zeeman splitting on the EEI correction that also results in a dip in the zero-field magnetoresistance, but is insensitive to the magnetic field direction at low fields (29, 31). Having established that the low field magnetoresistance behavior is dominated by WAL effect, we investigate the scattering mechanisms in these films using the Hikami-Larkin-Nagaoka (HLN) theory (32) applicable for a 2D electronic system, given by

$$\Delta G_{\text{WAL}}(B) = \alpha \frac{e^2}{\pi h} \left[ \frac{1}{2} \left( \Psi\left(\frac{1}{2} + \frac{B_\phi}{B}\right) - \ln\left(\frac{B_\phi}{B}\right) \right) - \frac{3}{2} \left( \Psi\left(\frac{1}{2} + \frac{\frac{4}{3}B_{\text{SO}} + B_\phi}{B}\right) - \ln\left(\frac{\frac{4}{3}B_{\text{SO}} + B_\phi}{B}\right) \right) \right] \quad (3)$$



where  $B_0$  and  $B_{SO}$  are the characteristic fields corresponding to electron dephasing and spin-orbit scattering, respectively, and  $\Psi(x)$  is the digamma function. Fits to the magnetoconductance data are shown in Fig. 6 (E and F), and extracted temperature dependence of the characteristic dephasing field  $B_0$  for the 12- and 6-ML films is shown in Fig. 6 (G and H), respectively. At 2 K, the phase coherence lengths ( $l_0$ ) were found to be 193 and 47 nm and the spin-orbit scattering lengths ( $l_{SO}$ ) 11 and 10 nm for the 12- and 6-ML-thick films, respectively (19). Temperature dependences of  $l_0$  and  $l_{SO}$  are shown in fig. S6A. Temperature dependence of  $B_0$  can be well-approximated as

$$B_0 = B_0 + B_{ee} + B_{eph} = a + bT + cT^n \quad (4)$$

where  $B_0$ ,  $B_{ee}$ , and  $B_{eph}$  are contributions due to impurity, electron-electron, and electron-phonon scattering, respectively;  $a$ ,  $b$ , and  $c$  are constants; and  $n$  varies between 2 and 4 (33). For the 12-ML-thick film at low temperatures, electron-electron scattering dominates, which is quickly overshadowed by contributions from the electron-phonon scattering at higher temperatures exhibiting a  $T^{2.2}$  dependence. However, for the 6-ML-thick film,  $B_0$  shows a linear temperature dependence suggesting the predominance of EEI effects in thinner films and also much weaker electron-phonon scattering. Our observation thus explains the origin of resistivity upturn at low temperatures in these films despite the absence of a bulk bandgap.

In summary, we have shown how magnetoresistance behavior can be modified and charge compensation can be lifted in an otherwise compensated semimetallic system by dimensionally confining charge carriers in ultrathin films. This approach has allowed us to distinguish the underlying mechanism behind the observed magnetoresistance behavior while establishing the efficacy of few atomic layer geometries in controlling electronic properties, which can be readily extended to other semimetallic systems. Although the presence of surface states at the interface between a rock salt and a zinc blende crystal structure (34–36) had been speculated in earlier studies, our experimental and theoretical work established the presence of a 2D hole gas at this technologically relevant heterointerface (37) and also elucidated its origin, which significantly affects the electronic and transport properties in the ultrathin limit. We have shown that controlling the nature of chemical bonding at the interface offers a novel route to realize 2D hole gas, which is distinct from a traditional 2D hole gas that arises because of the formation of accumulation layer near the interface as a result of band bending in semiconductors. Such emergent interfacial 2D hole or electron gas is expected to be generic in heterointerfaces with different bonding configurations and can profoundly influence advanced device geometries including those currently under investigation for topological quantum computing (38). No evidence for the lifting of semimetallicity is found in these thin heteroepitaxial films. However, our analysis of QI and EEI effects establishes the inadequacy of transport measurements alone in understanding either the predicted semimetallic to semiconducting phase transition or the evolution of the electronic structure with film thickness. Our work provides a comprehensive understanding of the electronic structure in ultrathin semimetallic systems that will be important in possible device applications (39) and in the realization of novel physical properties that are proposed to emerge in the ultrathin limit (2, 4, 40, 41). Our work also sets the stage for further control over their electronic properties by applications of biaxial stress and proximity effect in artificial heterostructures.

## MATERIALS AND METHODS

### Growth

Thin films were grown by MBE in a MOD Gen II growth chamber. A 5-nm-thick GaSb buffer layer was grown on low n-type doped GaSb (001) substrates (carriers freeze out at low temperatures; see fig. S2A) at 450°C under  $Sb_4$  overpressure after desorption of the native oxide using atomic hydrogen. This is followed by coevaporation of Lu and Sb from calibrated effusion cells with the substrate temperature at 380°C and the Lu to Sb flux ratio 1:1.10. The atomic fluxes of Lu and Sb are calibrated by Rutherford backscattering spectrometry measurements of the elemental areal density of calibration samples on Si. These measurements were used to calibrate in situ beam flux measurements using an ion gauge. The sample surfaces were protected with a 5-nm-thick AlOx layer using electron-beam evaporation before taking them out of the ultrahigh vacuum (UHV) chamber. For ARPES measurements, conductive n-type Te doped GaSb (001) substrates were used. Similar growth procedure was followed in our earlier work, as described in (12).

### HAADF-STEM

For the structural analysis using STEM, cross-sectional lamellas were prepared using a FEI Helios Dual-beam Nanolab 650 focused gallium ion beam (FIB) system. A 3- $\mu$ m-thick platinum (Pt) layer was deposited on the surface of the sample as a protective layer. Thereafter, FIB milling steps down to 2 kV were used to polish the lamella to approximately 50 nm in thickness. To minimize oxidation of the sample, the lamella was then immediately transferred to the STEM system. The HAADF-STEM imaging was carried out in a Thermo Fisher Scientific Talos G2 200X TEM/STEM system using the Thermo Fisher Scientific Velox software. The lamella was imaged along the GaSb [110] zone axis. A series acquisition was performed with a dwell time of 200 ns, and drift corrected frame integration (DCFI) was used to process the acquired images. Quantification of distances between atomic peaks in the STEM image was done using ImageJ and MATLAB software. Line intensity profiles (widths integrated over 5 pixels) were acquired at the center of the required atomic columns. Intensity profiles over 10 to 15 columns, having the same atomic configuration, were averaged to get final atomic profiles with high signal-to-noise ratio. Gaussian peak fitting was used to identify peak positions and calculate Lu-Lu or Sb-Sb atomic distances.

### Transport measurements

Following similar procedure described in our previous work (12), transport measurements were performed on fabricated Hall bar devices using standard ac lock-in technique at low temperatures with the current flowing along [110] crystallographic direction, where parallel conduction from the substrate and the buffer layers can be neglected at low temperatures (see fig. S2, A to C). The Hall bars were fabricated using standard optical lithography, followed by an ion milling procedure using argon ions. The contacts were made using 50- $\mu$ m gold wire bonded onto gold pads. Low temperature measurements were carried out in a Quantum Design PPMS with a base temperature of 2 K and a maximum magnetic field of 14 T.

### Angle-resolved photoemission spectroscopy

Samples were transferred in a custom-built vacuum suitcase from the growth chamber at Santa Barbara to the ARPES endstation 10.0.1.2 at the Advanced Light Source in Berkeley. The pressure inside

the vacuum suitcase was better than  $1 \times 10^{-10}$  torr. Tunable synchrotron light in the 20- to 80-eV range was used for the photoemission measurements with a Scienta R4000 analyzer. The base pressure of the analysis chamber was better than  $5 \times 10^{-11}$  torr. Similar sample transfer and ARPES measurement conditions were followed in our earlier work, as described in (12).

## DFT calculations

First-principles calculations, based on the DFT and projector augmented wave (42) method as implemented in the Vienna ab initio simulation package (VASP) code (43, 44), were carried out to study the electronic structure of the LuSb/GaSb (001) interface. For the exchange and correlation, we used the generalized GGA of Perdew-Burke-Ernzerhof (45). Test calculations based on the screened hybrid functional HSE06 (46, 47) were used to overcome the problem of DFT-GGA in overestimating the overlap of the electron and hole pockets in LuSb (12, 48) and underestimating the bandgap of GaSb. The effects of spin-orbit coupling are included in all band structure calculations. More details on the calculations can be found in the Supplementary Materials (section S4 and figs. S7 to S9) (19). The LuSb/GaSb (001) interface was simulated using (i) a slab geometry with LuSb/GaSb/LuSb layers with 7.5 layers of Ga-terminated GaSb sandwiched between two 6-ML-thick LuSb with a  $\sim 15$ -Å-thick vacuum layer (Fig. 5) and (ii) a LuSb/GaSb (001) superlattice with 17 layers of LuSb and 7.5 layers of GaSb without any vacuum layer (fig. S9). In both cases, there are two equivalent LuSb/Ga-terminated interfaces, which are rotated by  $90^\circ$  with respect to each other. LuSb (001) thin films were simulated using periodic slabs with 7, 13, 21, and 41 ML. The odd numbers of layers are chosen to ensure inversion symmetry, making it easier to analyze the band structures. These calculations were performed using the DFT-GGA functional with  $12 \times 12 \times 1$  special  $k$ -points; HSE06 calculations for these slabs are prohibitively expensive given the size of the supercell and the large number of  $k$ -points required to describe metallic systems. The results are shown in fig. S8. We note that the electron pocket at  $\Gamma$  seen in the bulk (fig. S7) and in the surface band structures (fig. S8) are projections of the electron pockets at the  $X_3$  in the bulk primitive cell (2 atoms per cell) that is folded to  $\Gamma$  point when using the four-atom tetragonal unit cell of LuSb (001) and the slabs.

## SUPPLEMENTARY MATERIALS

Supplementary material for this article is available at <http://advances.sciencemag.org/cgi/content/full/7/16/eabe8971/DC1>

## REFERENCES AND NOTES

- N. Armitage, E. Mele, A. Vishwanath, Weyl and Dirac semimetals in three-dimensional solids. *Rev. Mod. Phys.* **90**, 015001 (2018).
- J. Ruan, S. K. Jian, H. Yao, H. Zhang, S.-C. Zhang, D. Xing, Symmetry-protected ideal Weyl semimetal in HgTe-class materials. *Nat. Commun.* **7**, 1 (2016).
- S. Chadov, X. Qi, J. Kübler, G. H. Fecher, C. Felser, S.-C. Zhang, Tunable multifunctional topological insulators in ternary Heusler compounds. *Nat. Mater.* **9**, 541–545 (2010).
- Z. Li, J. Kim, N. Kiousis, S.-Y. Ning, H. Su, T. litaka, T. Tohyama, X. Yang, J.-X. Zhang, GdN thin film: Chern insulating state on square lattice. *Phys. Rev. B* **92**, 201303 (2015).
- F. F. Tafti, Q. D. Gibson, S. K. Kushwaha, N. Haldolaarachchige, R. J. Cava, Resistivity plateau and extreme magnetoresistance in LaSb. *Nat. Phys.* **12**, 272–277 (2016).
- F. F. Tafti, Q. Gibson, S. Kushwaha, J. W. Krizan, N. Haldolaarachchige, R. J. Cava, Temperature–field phase diagram of extreme magnetoresistance. *Proc. Natl. Acad. Sci. U.S.A.* **113**, E3475–E3481 (2016).
- T. Liang, Q. Gibson, M. N. Ali, M. Liu, R. J. Cava, N. P. Ong, Ultrahigh mobility and giant magnetoresistance in the Dirac semimetal  $\text{Cd}_3\text{As}_2$ . *Nat. Mater.* **14**, 280–284 (2015).
- I. A. Leahy, Y.-P. Lin, P. E. Siegfried, A. C. Treglia, J. C. W. Song, R. M. Nandkishore, M. Lee, Nonsaturating large magnetoresistance in semimetals. *Proc. Natl. Acad. Sci. U.S.A.* **115**, 10570–10575 (2018).
- J. Xu, N. J. Ghimire, J. S. Jiang, Z. L. Xiao, A. S. Botana, Y. L. Wang, Y. Hao, J. E. Pearson, W. K. Kwok, Origin of the extremely large magnetoresistance in the semimetal YSb. *Phys. Rev. B* **96**, 075159 (2017).
- L.-K. Zeng, R. Lou, D.-S. Wu, Q. N. Xu, P.-J. Guo, L.-Y. Kong, Y.-G. Zhong, J.-Z. Ma, B.-B. Fu, P. Richard, P. Wang, G. T. Liu, L. Lu, Y.-B. Huang, C. Fang, S.-S. Sun, Q. Wang, L. Wang, Y.-G. Shi, H. M. Weng, H.-C. Lei, K. Liu, S.-C. Wang, T. Qian, J.-L. Luo, H. Ding, Compensated semimetal LaSb with unsaturated magnetoresistance. *Phys. Rev. Lett.* **117**, 127204 (2016).
- J. Hu, T. F. Rosenbaum, Classical and quantum routes to linear magnetoresistance. *Nat. Mater.* **7**, 697–700 (2008).
- S. Chatterjee, S. Khalid, H. S. Inbar, A. Goswami, F. C. de Lima, A. Sharan, F. P. Sabino, T. L. Brown-Heft, Y.-H. Chang, A. V. Fedorov, D. Read, A. Janotti, C. J. Palmström, Weak antilocalization in quasi-two-dimensional electronic states of epitaxial LuSb thin films. *Phys. Rev. B* **99**, 125134 (2019).
- O. Pavlosiuk, M. Kleinert, P. Swatek, D. Kaczorowski, P. Wiśniewski, Fermi surface topology and magnetotransport in semimetallic LuSb. *Sci. Rep.* **7**, 12822 (2017).
- V. Sandomirskii, Quantum size effect in a semimetal film. *Sov. Phys. JETP* **25**, 101 (1967).
- H. L. Stormer, D. C. Tsui, A. C. Gossard, The fractional quantum Hall effect. *Rev. Mod. Phys.* **71**, S298–S305 (1999).
- A. Ohtomo, H. Y. Hwang, A high-mobility electron gas at the  $\text{LaAlO}_3/\text{SrTiO}_3$  heterointerface. *Nature* **427**, 423–426 (2004).
- A. Sharan, Z. Gui, A. Janotti, Formation of two-dimensional electron and hole gases at the interface of half-Heusler semiconductors. *Phys. Rev. Mater.* **3**, 061602 (2019).
- M. Przybylska, A. H. Reddoch, G. J. Ritter, The preparation and structure of Lutetium Diboride, Scandium Dodecaboride and Lutetium Antimonide. *J. Am. Chem. Soc.* **85**, 407–411 (1963).
- Supplementary Materials
- T.-C. Chiang, Photoemission studies of quantum well states in thin films. *Surf. Sci. Rep.* **39**, 181–235 (2000).
- R. Kudrawiec, H. P. Nair, M. Latkowska, J. Misiewicz, S. R. Bank, W. Walukiewicz, Contactless electroreflectance study of the Fermi level pinning on GaSb surface in n-type and p-type GaSb Van Hoof structures. *J. Appl. Phys.* **112**, 123513 (2012).
- P. W. Chye, I. Lindau, P. Pianetta, C. M. Garner, C. Y. Su, W. E. Spicer, Photoemission study of Au Schottky-barrier formation on GaSb, GaAs, and InP using synchrotron radiation. *Phys. Rev. B* **18**, 5545–5559 (1978).
- P. W. Chye, I. Lindau, P. Pianetta, C. M. Garner, W. E. Spicer, Evidence for a new type of metal-semiconductor interaction on GaSb. *Phys. Rev. B* **17**, 2682–2684 (1978).
- K. Nishi, M. Yokoyama, S. Kim, H. Yokoyama, M. Takenaka, S. Takagi, Study on electrical properties of metal/GaSb junctions using metal-GaSb alloys. *J. Appl. Phys.* **115**, 034515 (2014).
- P. A. Murawala, B. M. Arora, On the barrier height of Schottky diodes of Au on n-GaSb. *J. Appl. Phys.* **29**, L2434–L2437 (1990).
- B. Rotelli, L. Tarricone, E. Gombia, R. Mosca, M. Perotin, Photoelectric properties of GaSb Schottky diodes. *J. Appl. Phys.* **81**, 1813–1819 (1997).
- M. Altarelli, J. C. Maan, L. L. Chang, L. Esaki, Electronic states and quantum Hall effect in GaSb-InAs-GaSb quantum wells. *Phys. Rev. B* **35**, 9867–9870 (1987).
- V. Mokerov, Y. V. Fedorov, A. Hook, High density 2DEG in III-V semiconductor heterostructures and high-electron-mobility transistors based on them. *Sem. Ther.* **33**, 970–971 (1999).
- P. A. Lee, T. V. Ramakrishnan, Disordered electronic systems. *Rev. Mod. Phys.* **57**, 287–337 (1985).
- B. L. Altshuler, A. G. Aronov, P. Lee, Interaction effects in disordered Fermi systems in two dimensions. *Phys. Rev. Lett.* **44**, 1288–1291 (1980).
- B. L. Altshuler, A. G. Aronov, Electron–electron interaction in disordered conductors, in *Modern Problems in Condensed Matter Sciences* (Elsevier, 1985), vol. 10, pp. 1–153.
- S. Hikami, A. I. Larkin, Y. Nagaoka, Spin-orbit interaction and magnetoresistance in the two dimensional random system. *Prog. Theor. Phys.* **63**, 707–710 (1980).
- J.-J. Lin, J. P. Bird, Recent experimental studies of electron dephasing in metal and semiconductor mesoscopic structures. *J. Phys. Condens. Matter* **14**, R501–R596 (2002).
- C. C. Bomberger, B. E. Tew, M. R. Lewis, J. M. Zide, Growth and characterization of TbAs films. *Appl. Phys. Lett.* **109**, 202104 (2016).
- E. M. Krivoy, H. P. Nair, A. M. Crook, S. Rahimi, S. J. Maddox, R. Salas, D. A. Ferrer, V. D. Dasika, D. Akinwande, S. R. Bank, Growth and characterization of LuAs films and nanostructures. *Appl. Phys. Lett.* **101**, 141910 (2012).
- D. C. Driscoll, M. Hanson, C. Kadow, A. C. Gossard, Electronic structure and conduction in a metal–semiconductor digital composite: ErAs: InGaAs. *Appl. Phys. Lett.* **78**, 1703–1705 (2001).
- C. Palmström, S. Mounier, T. Finstad, P. Miceli, Lattice-matched  $\text{Sc}_{1-x}\text{Er}_x\text{As}/\text{GaAs}$  heterostructures: A demonstration of new systems for fabricating lattice-matched metallic compounds to semiconductors. *Appl. Phys. Lett.* **56**, 382–384 (1990).
- Y. Liu, S. Vaitiekėnas, S. Martí-Sánchez, C. Koch, S. Hart, Z. Cui, T. Kanne, S. A. Khan, R. Tanta, S. Upadhyay, M. E. Cachaza, C. M. Marcus, J. Arbiol, K. A. Moler, P. Krogstrup,



- Semiconductor–Ferromagnetic Insulator–Superconductor Nanowires: Stray field and exchange field. *Nano Lett.* **20**, 456–462 (2019).
39. C. C. Bomberger, M. R. Lewis, L. R. Vanderhoef, M. F. Doty, J. M. Zide, Review Article: Overview of lanthanide pnictide films and nanoparticles epitaxially incorporated into III-V semiconductors. *J. Vac. Sci. Technol. B* **35**, 030801 (2017).
  40. S. Khalid, F. P. Sabino, A. Janotti, Topological phase transition in LaAs under pressure. *Phys. Rev. B* **98**, 220102 (2018).
  41. H. Inoue, M. Han, M. Hu, T. Suzuki, J. Liu, J. G. Checkelsky, Band engineering of a magnetic thin film rare-earth monpnictide: A platform for high Chern number. *Phys. Rev. Mater.* **3**, 101202 (2019).
  42. P. E. Blöchl, Projector augmented-wave method. *Phys. Rev. B* **50**, 17953–17979 (1994).
  43. G. Kresse, J. Hafner, Ab initio molecular dynamics for liquid metals. *Phys. Rev. B* **47**, 558–561 (1993).
  44. G. Kresse, J. Hafner, Ab initio molecular-dynamics simulation of the liquid-metal–amorphous-semiconductor transition in Germanium. *Phys. Rev. B* **49**, 14251–14269 (1994).
  45. J. P. Perdew, K. Burke, M. Ernzerhof, Generalized gradient approximation made simple. *Phys. Rev. Lett.* **77**, 3865–3868 (1996).
  46. J. Heyd, G. E. Scuseria, M. Ernzerhof, Hybrid functionals based on a screened Coulomb potential. *J. Chem. Phys.* **118**, 8207–8215 (2003).
  47. J. Heyd, G. E. Scuseria, M. Ernzerhof, Erratum: “Hybrid functionals based on a screened Coulomb potential” [*J. Chem. Phys.* **118**, 8207 (2003)]. *J. Chem. Phys.* **124**, 219906 (2006).
  48. S. Khalid, A. Sharan, A. Janotti, Hybrid functional calculations of electronic structure and carrier densities in rare-earth monpnictides. *Phys. Rev. B* **101**, 125105 (2020).
  49. J. Bharathan, J. Narayan, G. Rozgonyi, G. E. Bulman, Poisson ratio of epitaxial Germanium films grown on Silicon. *J. Electron. Mater.* **42**, 40–46 (2013).
  50. S. H. Mir, P. C. Jha, M. S. Islam, A. Banerjee, W. Luo, S. D. Dabhi, P. K. Jha, R. Ahuja, Static and dynamical properties of heavy actinide monpnictides of Lutetium. *Sci. Rep.* **6**, 29309 (2016).
- Development of the growth facilities and low-temperature magnetotransport measurements were supported by the Office of Naval Research through the Vannevar Bush Faculty Fellowship under the award no. N00014-15-1-2845. Scanning probe studies were supported by NSF (award number DMR-1507875). This research used resources of the Advanced Light Source, which is a DOE Office of Science User Facility under contract no. DE-AC02-05CH11231. We acknowledge the use of shared facilities of the NSF Materials Research Science and Engineering Center (MRSEC) at the University of California Santa Barbara (DMR 1720256) and the LeRoy Eyring Center for Solid State Science at Arizona State University. A portion of this work was performed in the UCSB Nanofabrication Facility, an open access laboratory. DFT calculations made use of the National Energy Research Scientific Computing Center (NERSC), a U.S. Department of Energy Office of Science User Facility operated under contract no. DE-AC02-05CH11231. D.R. gratefully acknowledges support from the Leverhulme Trust via an International Academic Fellowship (IAF-2018-039). **Author contributions:** S.C. and C.J.P. conceived the study. Thin film growth, film characterization, and transport measurements were performed by S.C. with assistance from H.S.I., T.G., and D.R. DFT calculations were performed by S.K. under the supervision of A.J. ARPES measurements were performed by S.C. with assistance from H.S.I., D.R., Y.-H.C., E.Y., and A.V.F. and analyzed by S.C. TEM measurements and analysis were performed by A.G. The manuscript was prepared by S.C., S.K., A.J., and C.J.P. All authors discussed results and commented on the manuscript. **Competing interests:** The authors declare that they have no competing interests. **Data and materials availability:** All data needed to evaluate the conclusions in the paper are present in the paper and/or the Supplementary Materials. Additional data related to this paper may be requested from the corresponding author(s).
- Submitted 22 September 2020  
Accepted 25 February 2021  
Published 14 April 2021  
10.1126/sciadv.abe8971

#### Acknowledgments

**Funding:** Synthesis of thin films, development of the UHV suitcase, ARPES experiments, and theoretical work were supported by the U.S. Department of Energy (contract no. DE-SC0014388).

**Citation:** S. Chatterjee, S. Khalid, H. S. Inbar, A. Goswami, T. Guo, Y.-H. Chang, E. Young, A. V. Fedorov, D. Read, A. Janotti, C. J. Palmström, Controlling magnetoresistance by tuning semimetallicity through dimensional confinement and heteroepitaxy. *Sci. Adv.* **7**, eabe8971 (2021).

## Controlling magnetoresistance by tuning semimetallicity through dimensional confinement and heteroepitaxy

Shouvik Chatterjee, Shoaib Khalid, Hadass S. Inbar, Aranya Goswami, Taozhi Guo, Yu-Hao Chang, Elliot Young, Alexei V. Fedorov, Dan Read, Anderson Janotti and Chris J. Palmstrøm

*Sci Adv* 7 (16), eabe8971.  
DOI: 10.1126/sciadv.abe8971

### ARTICLE TOOLS

<http://advances.sciencemag.org/content/7/16/eabe8971>

### SUPPLEMENTARY MATERIALS

<http://advances.sciencemag.org/content/suppl/2021/04/12/7.16.eabe8971.DC1>

### REFERENCES

This article cites 48 articles, 2 of which you can access for free  
<http://advances.sciencemag.org/content/7/16/eabe8971#BIBL>

### PERMISSIONS

<http://www.sciencemag.org/help/reprints-and-permissions>

Use of this article is subject to the [Terms of Service](#)

*Science Advances* (ISSN 2375-2548) is published by the American Association for the Advancement of Science, 1200 New York Avenue NW, Washington, DC 20005. The title *Science Advances* is a registered trademark of AAAS.

Copyright © 2021 The Authors, some rights reserved; exclusive licensee American Association for the Advancement of Science. No claim to original U.S. Government Works. Distributed under a Creative Commons Attribution NonCommercial License 4.0 (CC BY-NC).